npj | climate and atmospheric science

Article

Published in partnership with CECCR at King Abdulaziz University

https://doi.org/10.1038/s41612-024-00644-y

A single-photon lidar observes atmospheric clouds at decimeter scales: resolving droplet activation within cloud base

Fan Yang [1] ✉, Alex B. Kostinski [2], Zeen Zhu[1], Katia Lamer[1], Edward Luke [1], Pavlos Kollias[1,3], Yong Meng Sua [4], Pei Hou[2], Raymond A. Shaw [2] & Andrew M. Vogelmann [1]

Clouds, crucial for understanding climate, begin with droplet formation from aerosols, but observations of this fleeting activation step are lacking in the atmosphere. Here we use a time-gated time-correlated single-photon counting lidar to observe cloud base structures at decimeter scales. Results show that the air–cloud interface is not a perfect boundary but rather a transition zone where the transformation of aerosol particles into cloud droplets occurs. The observed distributions of first-arriving photons within the transition zone reflect vertical development of a cloud, including droplet activation and condensational growth. Further, the highly resolved vertical profile of backscattered photons above the cloud base enables remote estimation of droplet concentration, an elusive but critical property to understanding aerosol–cloud interactions. Our results show the feasibility of remotely monitoring cloud properties at submeter scales, thus providing much-needed insights into the impacts of atmospheric pollution on clouds and aerosol-cloud interactions that influence climate.

Droplets formed from aerosol particles are the fundamental building blocks of atmospheric clouds, with subsequent climate effects on precipitation and the Earth's radiative energy budget[1–3]. The response of cloud properties to changes in aerosol loading from anthropogenic or natural emissions, known as aerosol-cloud interaction, is one of the largest uncertainties in future climate projections[4–7]. One key microphysical process related to aerosol-cloud interaction is the activation of aerosol particles through condensation to form cloud droplets at the cloud base where droplet concentration is initialized; namely, what happens at the cloud base influences the microphysical properties throughout the cloud[8]. For example, increasing aerosol number concentration can increase cloud droplet number concentration and decrease droplet size for the same liquid water content; this would increase cloud albedo and lead to cooling that can compensate for greenhouse warming[9,10]. Cloud droplet number concentration varies greatly, ranging from ~10 cm^{-3} in ultra-clean clouds to over 10^3 cm^{-3} in polluted clouds, depending on aerosol concentration[11], composition[12,13], size[14], updraft[15], and turbulence[16].

Despite their importance, detailed measurements of droplet formation at cloud bases remain challenging. In-situ observations require airborne platforms that are costly and limited in their spatiotemporal range, sampling volume, and detection efficiency of small droplets[17]. Ground-based remote sensing instruments with high temporal resolution have the advantage of continuously observing clouds at a much lower cost. In particular, atmospheric lidars firing visible and/or near-infrared laser pulses into the atmosphere are well-suited for the detection of micron-sized cloud droplets due to strong backscatter[18]. However, existing atmospheric lidars with range resolutions on the order of ten meters cannot resolve droplet formation processes[19]. Another fundamental challenge for cloud retrievals is that separation of droplet number from particle size using backscattered power is very difficult[20–22] or even impossible, as lidar backscatter is proportional to $n_d\bar{r}^2$, where n_d is droplet number concentration and $\bar{r}$ is the mean droplet radius. Hence, remote sensing has not yet delivered detailed observations of cloud microphysical properties and processes (e.g., droplet formation and growth) in the real atmosphere needed to fundamentally constrain aerosol-cloud interactions.

[1]Evironmental and Climate Sciences Department, Brookhaven National Laboratory, Upton 11973 NY, USA. [2]Department of Physics, Michigan Technological University, Houghton 49931 MI, USA. [3]School of Marine and Atmospheric Sciences, Stony Brook University, Stony Brook 11794 NY, USA. [4]Department of Physics, Stevens Institute of Technology, Hoboken 07030 NJ, USA. ✉e-mail: fanyang@bnl.gov

To address this observational gap, we developed a time-gated time-correlated single-photon counting lidar (hereafter referred to as T2 lidar) that can probe clouds with a vertical resolution that is two orders of magnitude finer than instruments commonly used—enhancing the resolution from 10 m down to 10 cm. This capability opens the door to remote sensing of droplet formation and subsequent growth within the cloud base. The technical details about the T2 lidar are described in ref. 19 and reviewed in the following section, while this study focuses on the scientific capabilities.

Results

T2 lidar technology overview

The ground-based, vertically pointing T2 lidar fires 532-nm wavelength laser pulses with a pulse width of 650 ps and a repetition rate of 20.6 kHz. The radiation emitted by the laser (hereafter referred to simply as "light") is expanded and collimated to a beam with a diameter of 90 mm to comply with eye safety requirements before it enters the atmosphere. The backscattered light is collected by a biaxial telescope with a diameter of 200 mm. The minimum overlap height between the laser-illuminated volume and the field of view of the telescope is about 750 m. The backscattered light goes through three optical filters before being measured by a single-photon-counting detector. The detector is synchronized with the most recent laser pulse, and the arrival time of each observed photon is recorded with an accuracy of 45 ps based on the time-correlated single photon counting technique[23]. The range resolution of the T2 lidar is processed afterward, and it is limited by the laser pulse width (650 ps), corresponding to about 10 cm. For comparison, other atmospheric lidars equipped with single-photon avalanche diode photon detectors usually use the multichannel scaler method to record photon counts, in which the range resolution is preset[24].

One feature of the T2 lidar is the application of a time-gating technique[19]. In the time-gated mode, the detector can receive photons only within a narrow time-gated window—this advanced observational capability allows us to zoom into a region of interest for cloud observations[19,25,26]. A digital delay pulse generator accepts a trigger pulse from the laser head and generates an output pulse. The digital delay generator is user-programmable for delay (0–10 s) and width (0–85 ns) with a 10 ps resolution to trigger the single-photon-counting detector to only receive backscattered photons within a specific time-gated window. For example, if we set a delay of 10 μs (corresponding to 1500 m) and a width of 85 ns (corresponding to 12.75 m), we expect to only receive backscattered photons between 1500 m and 1512.75 m. Because the dead time of the detector is about 50 ns, it is unlikely to receive more than one photon within the time-gated window after firing one laser pulse.

There are two advantages of the T2 lidar when operated in the time-gated mode. First, the detector can efficiently block photons outside the time-gated window, significantly increasing the signal-to-noise ratio. Second, T2 is unlikely to receive more than one photon within the time-gated window after firing a single laser pulse because of the detector's dead time, the latter comparable to window duration. Therefore, for nighttime observations (like in this study), most photons received by the T2 lidar are first-arriving backscattered photons within the time-gated window; in other words, the T2 lidar can do first-photon imaging of clouds[27]. In this manner, the T2 lidar achieves cloud observations at a decimeter resolution (~10 cm). We will also show later that the first-arriving photon statistics can provide valuable information on cloud microphysical properties.

T2 lidar observations of cloud base structure and droplet activation

A boundary layer stratiform cloud used in our analysis was observed on July 5, 2022 at the Brookhaven National Laboratory Center for Multiscale Applied Sensing observational site (40.8656 N, −72.8815 W, https://www.bnl.gov/cmas/). All observations were done after sunset, around 20:30 (local time, LT), to avoid confusion with sunlight. The cloud base height measured by a Vaisala ceilometer was about 1.7 km, and the cloud base region was scanned by the co-located T2 lidar around the same time (see Supplementary Fig. 1). By progressively delaying the time to open the time-gated window we can scan upwards through the cloud in the following way: First, we open an 85-ns time-gated window (corresponding to 12.75 m) at about 1.65 km and observe for 1 s. Then, the time-gated observation window is shifted upward by 1.5 m (corresponding to a 10 ns delay in time) for another 1-s observation, and so forth, until it reaches about 1.8 km. The arrival times of the backscattered photons in each time-gated window are binned to 1 ns, corresponding to a 15 cm range resolution.

The distributions of observed photons within the time-gated window exhibit distinct sub-meter features at different locations near the cloud base (Fig. 1a). Below the cloud, backscattered photons are randomly distributed within the 12.75-m time-gated window, and the photon rate is below 50 per second per 15-cm range sample. Transitioning into the cloud base, the backscattered photon rate increases significantly towards the end of the time-gated window, from less than 50 to about 250 per second, due to larger lidar backscatter by comparatively large cloud droplets, thereby instrumentally resolving the cloud base. Just above the cloud base, the photon rate peaks in the front of the window, but then the slope flattens farther above due to light extinction. These features can be clearly seen from the fraction of observed photons in each 15-cm range sample in four chosen time-gated windows (i.e., ratio of observed photons in each 15-cm range sample to the total observed photons in the time-gated window) (Fig. 1b). The fully resolved cloud bottom shows that the air-cloud interface is not a perfect boundary but, rather, is a transition zone, reminiscent of the "twilight zone" near cloud edges[28]. Thus, cloud base is a nebulous notion, yet its texture is used later to retrieve droplet concentration.

The T2 lidar can also observe highly resolved profiles of backscatter intensity. This is because the observed first-arriving backscattered photon rate in the front of a time-gated window is directly proportional to backscatter intensity. Figure 1c shows the profile of the observed photon rate within the first 1.5 m of each time-gated window. The slight increase in photon rate from 1.65 to 1.67 km implies the hygroscopic growth of aqueous solution droplets (commonly known as haze particles) toward cloud base[29], while the sharp increase in photon rate between 1.67 and 1.70 km indicates the activation and early growth of cloud droplets from the haze particles by condensation. T2 resolves the droplet activation zone near the cloud base and it can remotely measure the depth of the droplet activation layer. The activation layer is a few tens of meters in this case, which is supported by early observations of a stratiform cloud from a slowly ascending aircraft (see Figs. 8 and 9 in ref. 30). The decrease in photon rate above 1.70 km is a result of the extinction of backscatter intensity by the intervening cloud. These features presented in Fig. 1 are representative of other cloud observations by the T2 lidar (Supplementary Fig. 2). Next, we develop two minimal models to relate the observed first-arriving photons to cloud microphysical properties, serving as benchmarks for understanding T2 lidar observations.

Minimal models

Atmospheric lidars miss photon counts during the detector's dead time, and correction is needed to obtain the lidar backscattering profile[31]. In contrast (and perhaps paradoxically), our T2 lidar takes advantage of the relatively long detector's dead time to filter within the time-gated window, thereby disentangling first-arriving photons from the rest. Therefore, for a single laser pulse fired, the photon count takes on only two possible values: 0 or 1. Based on this binary character of arriving photons, below we develop a closed-form expression (see Eq. (2)) to quantify the distributions of detected photons via the *fraction* of these photons, originating from a given layer i and denoted by $F(i)$ as shown in Fig. 1b. We further develop an analytical formula to estimate droplet number concentration (see Eq. (11) below) based on the highly resolved profile of observed backscattered photons above the cloud (Fig. 1c).

First-arriving photon statistics. We now derive a minimal model that captures the dependence of the fraction of the first-arriving photons, denoted by $F(i)$, on the scattering by particles from the (sub)layer i observed within the time-gated window (e.g., Fig. 1b). Although in a single pulse (experiment), the location of the observed first-arriving

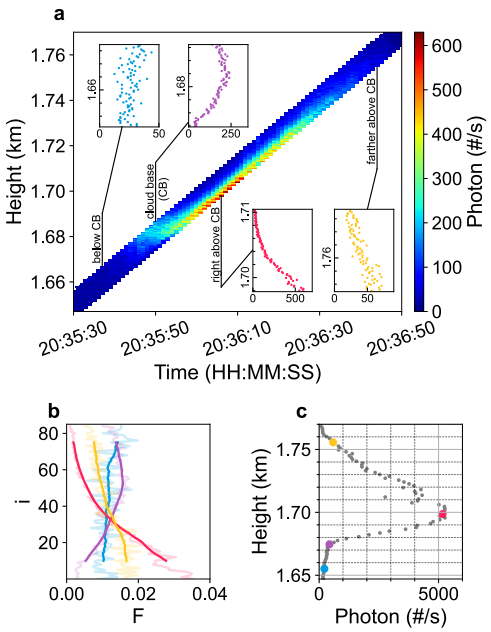

Fig. 1 | Observation of cloud vertical structure via scanning by the T2 lidar. The cloud was observed around 20:35 LT after sunset on July 5, 2022 at the Brookhaven National Laboratory Center for Multiscale Applied Sensing observational site. **a** The colored region shows the distribution of observed photons within a 12.75-m time-gated window (height of the insets) per second. The time-gated window starts below cloud base and shifts upwards by 1.5 m every second. Four inset plots show the distribution of observed photons at a 15-cm resolution within selected time-gated windows, namely below cloud base (CB), at CB, right above CB, and farther above CB. **b** Fraction $F(i)$ of observed photons within each sublayer i observed for the four selected time-gated windows in (**a**). The 12.75-m time-gated window is divided into 85 sublayers, each of thickness 15 cm. The thick lines show 20-point moving averages; the blue, red, and yellow lines are approximately linear, whose slopes are explained by the minimal model of first-arriving photons (see main text). **c** The profile of observed photon rate within the first 1.5 m of each time-gated window. The coloring of the dots in **a**–**c** corresponds to the four selected time-gated windows: blue for the haze region, purple marking the beginning of the haze-cloud transition, and red and yellow are both within the cloud. The relative backscatter (χ) of the yellow point is 11%, defined as the ratio of the observed photon rate at that level to its peak value in the profile.

backscattered photon originating in a time-gated window is a random variable (i.e., i), after 20k trials, the average profile is readily discernible. Figure 2 illustrates the theory of the statistics of first-arriving backscattered photons in a time-gated window.

Specifically, consider a time-gated window corresponding to a thickness H, divided into equal m sublayers, each of thickness l, the latter possibly as small as the lidar's range resolution (e.g., $l \sim 15$ cm in our case). Within a sublayer i (where $i = 1$ represents the first sublayer at the front of the time-gated window), there are n_i particles (e.g., aerosol, haze, or cloud droplets) responsible for the lidar backscatter. Particle j within sublayer i has a probability $p_{i,j}$ to generate one backscattered photon observed by the detector after firing a single laser pulse. We define an auxiliary variable, I_i, as the probability to generate one detectable backscattered photon from sublayer i. Then one obtains $I_i = 1 - \prod_{k=1}^{n_i}(1 - p_{i,k})$.

Because at most one photon is expected to be observed in the time-gated window after a single laser pulse due to the detector's deadtime, for nighttime observations, as in this study, the observed photons are first-arriving backscattered photons. The detection of one backscattered photon from sublayer i in response to a single pulse implies that no detection occurred from any other sublayers. Therefore, the probability of observing a first-arriving backscattered photon from the first sublayer is unity minus the probability of not detecting backscattered photons from any particle within the first sublayer, $P_1 = 1 - \prod_{k=1}^{n_1}(1 - p_{1,k})$. Note that P_1 is not affected by other sublayers because of the "first of the first" principle: first-arriving photons from the lowest sublayer travel least (see Fig. 2 middle panel). For $i > 1$, the probability of observing a first-arriving photon from sublayer i is the product of not receiving any photon below sublyaer i and receiving a photon at sublayer i,

$$P_i = \left[\prod_{s=1}^{i-1}\prod_{t=1}^{n_s}\left(1 - p_{s,t}\right)\right]\left[1 - \prod_{k=1}^{n_i}\left(1 - p_{i,k}\right)\right]. \quad (1)$$

Here, n_s is the total number of particle in the sublayer s. The interior product in the first bracket ($\prod_{t=1}^{n_s}\ldots$) represents the probability of not receiving backscattered photons from a single sublayer, and the exterior product in the first bracket ($\prod_{s=1}^{i-1}\ldots$) represents the probability of not receiving backscattered photons from sublayers 1 to $i-1$. The second square bracket represents the probability of receiving backscattered photons from sublayer i.

The fraction of the first-arriving photons in sublayer i within a time-gated window (containing m sublayers) is $F(i) = P_i / \sum_{j=1}^{m} P_j = \mu_i / \sum_{j=1}^{m} \mu_j$, where μ_i is the expected first-arriving photon counts from a sublayer i. Thus, by the law of large numbers, the fraction of observed average photon counts from a sublayer i within the window (e.g., Fig. 1b) approaches $F(i)$ for a large number of trials (20k pulses). For uniformly distributed droplets of a single size within a time-gated window, the fraction of the first-arriving photons reduces to (derived in Methods),

$$F(i) \approx -\frac{2q}{2m - m^2 q + mq} i + \frac{2+2q}{2m - m^2 q + mq} = Ai + B \quad (2)$$

The slope and intercept of the linear function, A and B, are linked to the physics via an experimentally based parameter, $q \equiv np_1 + \delta$, where n is the total number of particles in a single sublayer, and p_1 is the probability of receiving one backscattered photon from one particle in the first sublayer after firing a single laser pulse. Note that $p_{1,j}$ has been reduced to p_1 in Eq. (2) because all particles are identical (i.e., independent of the subscript j). Also, note that np_1 is analogous to the lidar backscattering coefficient[32], and the range-extinction parameter, $\delta \equiv 2(\sigma l + l/d)$, depends on the volume lidar extinction coefficient (σ, sum of the product of particle cross-section and extinction efficiency per unit volume), the thickness of the sublayer (l), and distance of the time-gated window from the lidar (d). The extinction efficiency can be calculated using a Mie code, while it is taken as a constant of 2 when deriving analytical models, which is the standard value used to calculate the optical properties of clouds in minimal models[33].

The approximate Eq. (2) captures the main features of T2 lidar observations, such as the blue, red, and yellow lines in Fig. 1b. The scattering of the T2 pulse below the cloud base is dominated by the weakly scattering haze/aerosol particles. Consequently, $np_1 \ll 1$ and all terms containing q in Eq. (2) can be neglected, and $F(i)$ collapses to $1/m$, i.e., a uniform distribution. Indeed, the blue line is close to the theoretical value of 0.012 ($1/m$ with $m = 85$ sublayers). Right above cloud base, because of strong scattering by cloud droplets, p_1 increases sharply, causing a negative slope from Eq. (2). This aligns with the observations that the photon rate peaks in front of the time-gated window (red line in Fig. 1b). Thereafter, because of extinction, p_1 decreases farther into the cloud, resulting in a flattening of the $F(i)$ profile (yellow line in Fig. 1b). Departures from linearity predicted by Eq. (2) would imply non-uniformities in microphysical properties within the time-gated window, such as gradients in droplet sizes (e.g., droplets grow sharply at the cloud base due to activation) and/or variations in concentration (e.g., droplet clustering due to turbulence, entrainment and mixing).

Highly resolved attenuation profile linked to droplet concentration. Next, we show that the high-resolution profile of backscattered photons observed by the T2 lidar (e.g., Fig. 1c) can be used to estimate cloud droplet number concentration (n_d). First, we expect that near the bottom of a boundary layer stratiform cloud where entrainment is negligible,

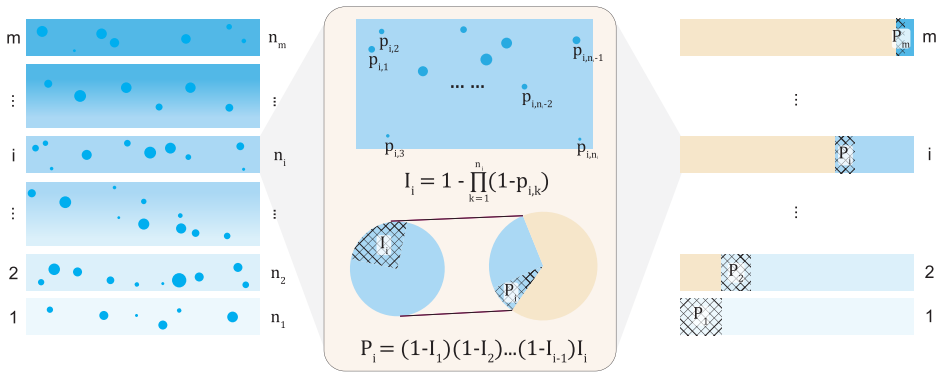

Fig. 2 | Schematic figure illustrating the theory of the statistics of first-arriving backscattered photons from a time-gated window. The left subplot shows a time-gated window divided to m sublayers, each contains n_i particles responsible for light scattering where i is the sublayer number. The zoom-in sublayer i in the middle indicates that each particle therein has a probability $p_{i,j}$ to generate a detectable backscattered photon in response to a single pulse, where i and j are sublayer and particle indices. The intermediate variable, I_i, represents the probability to generate a detectable backscattered photon from sublayer i, while P_i defined in Eq. (1) is the probability of observing a first-arriving backscattered photon from sublayer i. P_i is the product of the probability of not receiving backscattered photons before sublayer i and the probability of receiving backscattered photons at sublayer i. P_i can also be interpreted geometrically in the right subplot as the ratio of the hatched area to the whole bar area (i.e., light yellow + hatched blue + light blue). The fraction of the yellow area represents the probability of receiving first-arriving photons before that sublayer, i.e., $\sum_{k=1}^{i-1} P_k$.

cloud liquid water content (LWC) increases linearly with height as is commonly observed[34,35],

$$\frac{4}{3}\pi\rho_l n_d r^3 = \Gamma_{ad} z, \tag{3}$$

where r is droplet radius, which increases with height due to condensational growth, and z is the height above the cloud base. $\Gamma_{ad} = \Gamma_{ad}(T, P)$ is the rate of increase of LWC with height in an adiabatic cloud parcel, which is a function of temperature and pressure (see Eq. A1 in ref. 35). Here, LWC is the cloud mass density with units of g m^{-3} and it scales with the product of droplet concentration (n_d) which we assume to be constant above cloud base[36], and droplet volume ($4/3\pi r^3$).

Now consider a height z above the cloud base. The cloud optical depth between the cloud base (i.e., $z = 0$) and z is $\int_0^z 2\pi n_d r^2 dz$. Given that LWC increases linearly with height, differentiation of Eq. (3) yields $4\pi\rho_l n_d r^2 dr = \Gamma_{ad} dz$, and thus,

$$\int_0^z 2\pi n_d r^2 dz = \int_0^{r(z)} 2\pi n_d r^2 \frac{4\pi\rho_l n_d r^2}{\Gamma_{ad}} dr = \frac{8\pi^2\rho_l^2 n_d^2 r(z)^5}{5\Gamma_{ad}}, \tag{4}$$

where n_d and $r(z)$ here are droplet number concentration and size at z.

Another fact we rely on is how backscattered light is attenuated inside the cloud, which can provide another relationship between n_d and r other than Eq. (4). The observed photon rate at the front of the time-gated window does not suffer the detector's dead time, and thus it is proportional to the observed backscattered light intensity, or the observed backscattering coefficient ($\beta_{\rm obs}$). $\beta_{\rm obs}(z)$ at z above cloud base can be expressed as[33],

$$\beta_{obs}(z) = \beta_{true}(z)\exp\left(-2\int_0^z \sigma dz\right), \tag{5}$$

where $\beta_{\rm true}(z)$ is the true backscattering coefficient at z, and σ is the volume extinction coefficient. For the scattering of visible light by cloud droplets, it is reasonable to assume $\beta_{\rm true} = \sigma/S$ and $\sigma \approx 2\pi n_d r^2$, where S is the lidar ratio (extinction to backscatter ratio) and the extinction efficiency for light scattering by cloud droplets is taken as a constant of 2[33]. The contribution of multiple scattering to backscatter can be neglected because the phase function is sharply peaked in the forward direction, and the telescope of the T2 lidar has a narrow field of view (FOV ~ 0.5 mrad = 0.06°)[19,37,38].

Above the cloud base, $\beta_{\rm obs}$ first increases with height due to strong light backscattering by increasingly larger cloud droplets and then decreases with height due to light extinction (Fig. 1c). We define z_p as the height where $\beta_{\rm obs}$ reaches its peak value. By solving $d\beta_{\rm obs}/dz = 0$ and combining with Eq. (4), we obtain,

$$8\pi^2\rho_l n_d^2 r_p^5 = \Gamma_{ad}, \tag{6}$$

where r_p is the droplet radius at z_p.

Now we introduce a threshold value χ as the ratio of the observed backscattered light intensity at a higher level z_χ to its peak value at z_p (i.e., $z_\chi > z_p$),

$$\chi \equiv \frac{\beta_{obs}(z_\chi)}{\beta_{obs}(z_p)}, \tag{7}$$

$\beta_{obs}(z_\chi)$ can be set as low as the noise level. Thus,

$$\frac{n_d r_\chi^2 \exp(-2\int_0^{z_\chi} 2\pi n_d r^2 dz)}{n_d r_p^2 \exp(-2\int_0^{z_p} 2\pi n_d r^2 dz)} = \chi, \tag{8}$$

where r_p and r_χ are the droplet radius at z_p and z_χ, respectively. The height z_χ is an essential notion to developments below, and, for sufficiently small χ (say 1% or β at the top down to 1% of its peak value), it can be regarded as a lidar detectable range within the cloud.

We now show that n_d can be estimated for *any* τ_χ and z_χ pairs within the quasi-steady growth region. To that end, let the droplet radius at z_χ be k times larger than that at z_p, $r_\chi = kr_p (k > 1)$. Combining Eqs. (4) and (8) leads to an equation for k,

$$k^2 \exp\left[-\frac{2}{5}(k^5 - 1)\right] = \chi. \tag{9}$$

For a given χ, we can find the unique root k satisfying Eq. (9) for $k > 1$. Combining Eqs. (4) and (6), the cloud optical depth between the cloud base and z_χ can then be solved analytically,

$$\tau_\chi = \frac{8\pi^2\rho_l n_d^2 r_\chi^5}{5\Gamma_{ad}} = \frac{k^5}{5}, \tag{10}$$

which only depends on k. For example, if $\chi = 1\%$, the solution of Eq. (9) is $k \approx 1.724$, and the cloud optical depth at z_χ is about 3 (Eq. (10)). Therefore, for a given χ, we can get the relationship between n_d and r_χ at z_χ from

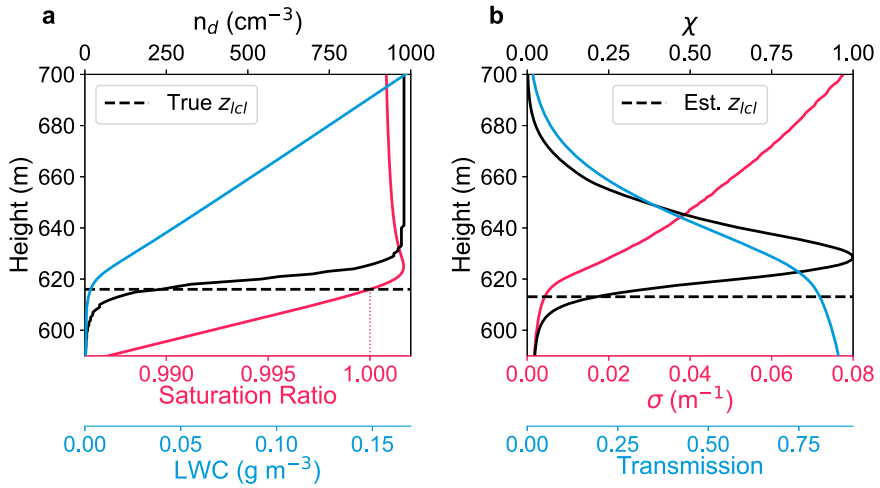

Fig. 3 | On the notion of cloud base: thermodynamic vs. kinetic. Results from a parcel model and a T2 lidar simulator. The case setup is detailed in the main text and Supplementary Table 1. **a** Profiles of air saturation ratio (red), liquid water content (LWC, blue), and droplet number concentration (n_d, black) for a rising cloud parcel. The horizontal dashed line denotes the thermodynamically defined sharp cloud base height (lifting condensation level, z_{lcl}), whereas the increase in n_d is continuous near z_{lcl}. Quasi-steady state growth is observed above 640 m where the LWC increases linearly with height, while n_d and the saturation ratio stay constant. **b** Simulated T2 lidar backscatter profile scaled by its peak value (χ, black). The horizontal dashed line denotes the T2-estimated z_{lcl} where the χ rate of increase is maximal. The scaled ratio χ peaks a few tens of meters above z_{lcl}, arising from the competition between the increasing scattering by larger droplets (i.e., extinction coefficient, σ) and the decreasing lidar intensity due to extinction (i.e., light transmission above the starting location of the parcel, $\exp(-\int_0^z \sigma dz)$) at a higher altitude.

Eq. (10). Solving for n_d based on Eqs. (3) and (10) results in,

$$n_d = \frac{2\rho_l^2 k^{15}}{243\pi\Gamma_{ad}^2 z_\chi^5}. \tag{11}$$

Combining Eqs. (10) and (11), we arrive at an analytic expression for n_d as,

$$n_d = \frac{250 l_{ad}^2}{243\pi}\frac{\tau_\chi^3}{z_\chi^5} \approx \left(\frac{l_{ad}^2}{3}\right)\frac{\tau_\chi^3}{z_\chi^5}, \tag{12}$$

where we introduce $l_{ad} = \rho_l/\Gamma_{ad}$, a length scale given by the ratio of water density (ρ_l with a unit of kg m^{-3}) to the adiabatic rate of increase in LWC with height (Γ_{ad} with a unit of kg m^{-3} m^{-1}). z_χ and τ_χ are the geometric thickness and the associated cloud optical depth, respectively. These two variables are pinned to values with a specific relative backscatter (χ), e.g., $\chi = 11\%$ yields $z_{0.11}$ and $\tau_{0.11}$ corresponding to the yellow dot in Fig. 1c.

The beauty of the n_d estimate via Eq. (12) is that so little is required other than the actual T2 observations. Namely, χ and z_χ can be read off directly and with high accuracy from the profiles of backscattered intensity (Fig. 1c). Furthermore, τ_χ can be calculated analytically (Eq. (10)). Finally, owing to the relative nature of χ, no absolute calibration of the lidar backscatter coefficient (β) is required to retrieve n_d, in contrast to traditional lidar-based retrievals[22,39]. Equation (12) allows any z_χ and τ_χ data pair to be used for estimating n_d.

To convey an intuitive appreciation of the magnitudes involved, we set $\chi = 1\%$ and obtain $\tau_{\chi=1\%} = 3$ by solving Eqs. (9) and (10). From there, we obtain Eq. (12): $n_d \approx 9.2 l_{ad}^2/z_\chi^5$. The dimensions on both sides now are manifestly (droplet) counts per volume. Because $l_{ad} \sim 5 \times 10^8$ m and $z_\chi \sim 10^2$ m, respectively, Eq. (12) yields a reasonable estimate of hundreds of droplets per cubic cm for n_d. A numerical cloud-resolving parcel model is used in the next section (see also Fig. 3) to provide detailed cloud profiles (e.g., LWC, n_d, χ) and confirm the derivation of Eq. (12).

Another remarkable feature of Eq. (12) is that $\tau \sim z^{5/3}$ for constant n_d. The nonlinear scaling arises from quasi-steady growth of the droplets above cloud base, where droplet radius r obeys $dr/dt \sim s_{qs}/r$ and quasi-steady supersaturation $s_{qs} \sim w/(n_d r)$, where w is the vertical velocity[40–42]. Integrating the droplet growth equation and using $wdt = dz$ yields $n_d r^3 \sim z$, showing a linear LWC increase with height. Because $\tau \sim n_d r^2 z$, we obtain $\tau^3 \sim z^5$ (n_d held constant).

Note that the scaling relationship of n_d with z_χ and τ from Eq. (12) also holds when the entire cloud layer is treated as a whole, i.e., z is cloud thickness (H_c) and τ is the total cloud optical depth. This is consistent with previous studies, $n_d = C(T,P)\tau_d^3 LWP^{-2.5}$ (Eq. (2) in ref. 43), where τ_d is the cloud optical depth and LWP is the liquid water path (i.e., height integral of LWC). Here, because $LWC \propto z$, therefore $LWP \propto H_c^2$ and, thus, $n_d \propto LWP^{-2.5} \propto H_c^{-5}$, consistent with Eq. (12).

Quantifying droplet concentration n_d

Because n_d scales with z_χ^{-5}, accurate measurements of cloud base height and z_χ are key to reliable n_d retrieval. However, the transition region near cloud base raises the question of where the cloud base boundary is. To answer this, a cloud-resolving model and a lidar simulator are employed to understand the T2 observations.

The cloud model simulates detailed cloud microphysical processes in a rising parcel, including hygroscopic growth of haze particles, cloud droplet activation, and growth of cloud droplets by condensation. The cloud model was originally developed by ref. 44 and has been applied to explore aerosol–cloud interactions under various environmental conditions[45,46]. A lognormal size distribution of dry ammonium sulfate aerosol particles is discretized and represented by 100 Lagrangian particles, which serve as model input. These dry aerosols first become haze particles through deliquescence at the beginning of the simulation and then grow in size by condensation in a rising adiabatic cloud parcel. The growth of haze particles and cloud droplets as well as the activation of cloud droplets from haze particles are resolved explicitly. To cover a wide range of atmospheric cloud conditions, we conduct 16 simulations with various combinations of vertical velocity (0.1 or 1.0 m s^{-1}), aerosol number concentration (50 or 1000 cm^{-3}), aerosol geometric mean radius (50 or 120 nm), and logarithmic radius (1.4 or 1.8). Model setups for each case are listed in Supplementary Table 1. Cloud microphysical properties are output every 10 cm to match the highest range resolution of the T2 lidar. Results show that cloud droplet number concentration depends on both vertical velocity (w) and aerosol properties consistent with previous studies[15]. n_d varies from less than 40 cm^{-3} in relatively clean conditions to 1000 cm^{-3} in relatively polluted conditions, covering a wide dynamic range observed in atmospheric clouds (Supplementary Fig. 3).

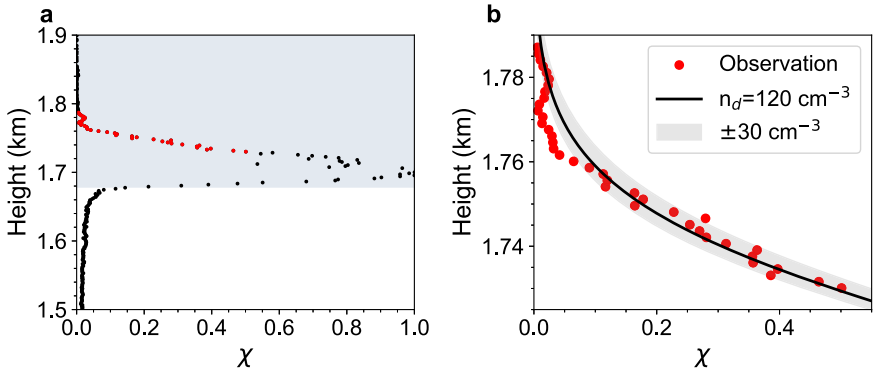

Fig. 4 | N_d estimates from T2 lidar observation. **a** The threshold ratio χ vs. height based on Fig. 1c. The white-gray boundary indicates the estimated cloud base height where the rate of increase in χ with height is maximized. The red dots for χ between 0.5% and 50% are used to independently estimate n_d via Eq. (12). **b** Best fitted curve suggests $n_d \approx 120$ cm^{-3}. The gray region indicates ±30 cm^{-3} from the best fit, where the upper bound associates with smaller n_d.

The T2 lidar simulator uses output from the parcel model to emulate distributions of first-arriving photons within the time-gated window. The time-gated window is set to be 10 m with 100 sublayers, each with a 10 cm range resolution. We calculate the backscatter and extinction coefficients in each sublayer based on the haze/droplet size distribution using a Mie scattering code. We define I_1 as the probability of generating one detectable backscattered photon from the first sublayer (see Fig. 2). From I_1, we can calculate the probability of having one detectable backscattered photon from any sublayer (I_i) based on the lidar equation, $I_i/I_1 = (d_1^2/d_i^2)(\beta_i/\beta_0)\exp(-\int_{d_1}^{d_i}\sigma_j dr_j)$ where β and σ are calculated using output from the parcel model via a Mie code and d is the distance from the lidar[10]. Therefore, the probability of receiving the first-arriving backscattered photons in a sublayer i within a time-gated window after one laser pulse (P_i) can then be calculated similarly to Eq. (1), which is only a function of I_1. We can constrain I_1 by the ratio of the observed total number of first-arriving photons in one time-gated window above the cloud base to the total number of fired pulses. For example, if we receive 10k photons within one time-gated window after firing 20k pulses per second, then $\sum P_i = 0.5$, and I_1 can be solved numerically. Once we know I_1, we can calculate I_i for any sublayer i. Simulated distributions of first-arriving photons are similar to the T2 lidar observations shown in Fig. 1a, suggesting that statistics of first-arriving photons within the time-gated window reveal the cloud microphysics therein (Supplementary Fig. 4).

Figure 3a shows one example of a simulated cloud from case 15 in Supplementary Table 1. Specifically, the initial temperature and pressure of the parcel are 15 °C and 919 hPa. The parcel has a relative humidity of 85%, and it rises from 300 m with a constant vertical velocity of 1.0 m s^{-1}. The initial dry aerosols are ammonium sulfate with a log-normal distribution with a total concentration of 1000 cm^{-3}, a geometric mean radius of 120 nm, and a logarithmic radius of 1.4. Results show that the lifting condensation level (z_{lcl}) serves as a good proxy for a thermodynamically defined cloud base height, where the parcel first becomes water-saturated. Above z_{lcl}, the air is supersaturated, leading to the formation and growth of cloud droplets by condensation. A quasi-steady state region is reached a few tens of meters above z_{lcl}. In this region, LWC increases linearly with height while n_d and supersaturation hold constant. Figure 3b shows the simulated χ profile, which is similar to the T2-observed χ profile (Fig. 4a). χ peaks a few tens of meters above z_{lcl} due to the competition between two things: the increasing scattering by larger cloud droplets and the decreasing lidar intensity due to extinction. Results of Fig. 3 show that the height where the χ rate of increase is a maximum agrees well with the lifting condensation level z_{lcl}.

Given this capability to infer z_{lcl} from T2 observations, we can now estimate n_d via Eq. (12) based on the observed χ profile (Fig. 4b). Cloud base height is estimated as the height with the maximum increase rate of χ, supported by modeling results discussed before. Temperature and pressure at cloud base height are 287 K and 834 hPa, estimated from reanalysis data (Supplementary Fig. 5). Based on Eq. (12), the best fit of χ between 0.5% and 50% yields an estimated $n_d \approx 120$ cm^{-3}. The coefficient of determination from the best-fitting curve is $R^2 = 0.97$, suggesting that the fine resolution of the observed photon rate profile provides a robust estimate of n_d. It is also encouraging that this estimate is consistent with the n_d estimate from another T2 lidar scan (≈117 cm^{-3}) on the same day (Supplementary Fig. 6). We further evaluate our n_d retrievals based on the simulated χ profiles calculated by the T2 lidar simulator using output from cloud parcel model simulations. Results show that the estimated n_d agrees reasonably well with the true n_d from the parcel model over a wide range (Supplementary Fig. 7). The only exception is when the cloud is extremely polluted with many large haze particles below z_{lcl}. In this case, z_{lcl} does not have a sharp boundary in terms of backscatter for the lidar to distinguish.

It should be mentioned that there are two main factors that can affect the accuracy of the n_d estimate based on Eq. (12). One factor comes from the uncertainties in the measurement of other variables, such as cloud base height (which can affect z_χ), and cloud temperature and pressure (which can affect Γ_{ad} or l_{ad}). It turns out that n_d is very sensitive to cloud base height. Taking the n_d estimate in Fig. 4 as an example, a 5 m increase in cloud base height leads to an increase in n_d by 55% (186 vs. 120 cm^{-3}), while a 2 K decrease in cloud temperature leads to an increase in n_d by 7% (128 vs. 120 cm^{-3}), all else being equal. Results suggest that it is critically important to measure the cloud base height (i.e., lifting condensation level) as accurately as possible. The other factor originates from the failure of assumptions we made when deriving Eq. (12). For example, the assumption of cloud adiabaticity near the cloud base might not hold due to various mechanisms, such as entrainment and mixing of dry air[47], radiative heating of the cloud layer[48], precipitation[49], and ascent of an air layer as a whole[50].

Recall that all observations reported in this study were conducted after sunset to avoid the influence of sunlight. The T2 lidar can operate in the daytime because it has an optical bandpass filter centered at 532.2 nm with a full width at a half maximum of 0.21 nm, which can efficiently block other unwanted wavelengths[19]. Although observations in this study are from a single night, the capability of the T2 lidar to observe fine cloud structure is broadly applicable to all cloud types. More T2-lidar observations are needed to understand the performance of the T2 lidar and to explore cloud base fine structures under various environmental conditions, which will be the focus of the future investigation. Our minimal models provide reference profiles to interpret the observed photon counts and link them to cloud microphysical properties.

Discussion

It is known that cloud droplets are initially formed from aerosol particles, but resolving droplet formation under atmospheric cloud conditions is challenging, which impedes understanding of cloud-aerosol interactions. So far, the only way to obtain detailed microphysical properties of atmospheric clouds has been through aircraft in-situ measurements, but the small sampling volume and fast-moving platform make it difficult to observe the vertical development of cloud microphysical properties at high resolution. The T2 lidar solves this problem by remotely sensing atmospheric clouds at submeter scales, thereby supplying a way to explore droplet formation and subsequent growth near the cloud base without disturbing the cloud environment. T2 provides a reliable way to remotely measure the depth of

the droplet activation layer, whose in-situ measurements are exceedingly scarce. Statistics of the first-arriving photons have been shown to provide insights of cloud microphysical properties within a time-gated window. The highly resolved profiles of backscattered photons above the cloud base indicate regions where droplets experience quasi-steady growth, and the trend in attenuation allows for the separation of n_d and r, which has been a fundamental challenge for traditional lidars.

High-resolution cloud observations can reveal insights into cloud properties at submeter scales. For example, two-dimensional cloud images captured by a high-resolution digital camera show variations in radiance and cloud optical depth at a resolution of ~1 cm[51]. In-situ measurements with a spatial resolution of ~10 cm from a slowly moving kite balloon indicate a sharp air-cloud interface near the cloud edge[52]. Here, high-resolution cloud vertical structure and droplet activation zone are resolved by the T2 lidar. Key attributes enabling the T2 lidar to resolve cloud texture at decimeter scales are short laser pulses, the time-gating technique, and a single-photon detection capability. Our study highlights the benefits of applying advanced technologies, well established in other fields, to observe atmospheric clouds at submeter scales, which can open up avenues for advancing our understanding of cloud microphysical properties and processes that are crucial to weather and climate.

Methods

Full derivation of Eq. 2 in the main text

If particles responsible for backscattered photons within a time-gated window are monodisperse and uniformly distributed, with n_i being constant for the different sublayers, the probability of receiving one backscattered photon from one particle after one laser pulse is the same in one sublayer (i.e., $p_{i,j} = p_i$). Thus, the probability of observing the first-arriving backscattered photons from the first sublayer is $P_1 = 1 - (1 - p_1)^n$, while for $i > 1$,

$$P_i = \left[\prod_{s=1}^{i-1}(1-p_s)^n\right]\left[1-(1-p_i)^n\right]. \tag{13}$$

The first bracket represents the probability of not receiving backscattered photons below sublayer i in the time-gated window, and the second bracket represents the probability of receiving backscattered photons from sublayer i. The fraction of first-arriving photons in sublayer i within the time-gated window ($F(i) = P_i / \sum_{j=1}^{m} P_j$) can be written as,

$$F(i) = \frac{\left[\prod_{s=1}^{i-1}(1-p_s)^n\right]\left[1-(1-p_i)^n\right]}{\sum_{j=1}^{m}\left[\prod_{s=1}^{j-1}(1-p_s)^n\right]\left[1-(1-p_j)^n\right]}. \tag{14}$$

The ratio of p_i in two adjacent sublayers can be linked by the lidar equation[33],

$$\frac{p_{i+1}}{p_i} = \frac{\beta_{i+1}}{\beta i}\frac{d_i^2}{d_{i+1}^2}\exp(-2\sigma l), \tag{15}$$

where β is the particle backscatter coefficient, σ is the particle extinction coefficient, d is the distance of the sublayer away from the lidar, and l is the thickness of the sublayer. Subscripts i and $i+1$ represent the sublayer i and the adjacent sublayer above. Because $\beta_i = \beta_{i+1}$ for monodisperse droplets, and $d_{i+1} = d_i + l$, and $l \ll d$, we obtain,

$$\frac{p_{i+1}}{p_i} \approx 1 - \delta \equiv A, \tag{16}$$

where $\delta \equiv 2l(\sigma + 1/d)$. Assuming A is roughly a constant within a narrow time-gated window, Eq. (14) can be simplified as,

$$F(i) \approx \frac{\left[\prod_{s=1}^{i-1}(1-A^{s-1}p_1)^n\right]\left[1-(1-A^{i-1}p_1)^n\right]}{\sum_{j=1}^{m}\left[\prod_{s=1}^{j-1}(1-A^{s-1}p_1)^n\right]\left[1-(1-A^{j-1}p_1)^n\right]}. \tag{17}$$

Here we show that the probability of receiving a photon from a single particle after a single T2 pulse is far below unity, $p_{i,j} \sim p_i \sim p \ll 1$, which enables simplifications to Eq. (17). Recall that p is an experimental variable that depends on the T2 characteristics (power and wavelength), the pulse intensity when arriving at the time-gated window (i.e., light intensity can be decreased due to scattering and absorption below the time-gated window), the microphysical properties of particles within the time-gated window (such as number, size, and shape), the efficiency of the lidar receiving system, and the integration time. We proceed to do a back-of-the-envelope calculation to demonstrate that $p \ll 1$ for the T2 lidar observations.

As Fig. 1c shows, we receive about 5k backscattered photons within a 1.5 m thick sampling volume (corresponding to 10 ns) after firing 20k pulses within one second (lidar repetition rate is 20.6 kHz). Because the diameter of the collimated beam after the beam expander is 9 cm and the droplet number concentration is on the order of $10^2\,\mathrm{cm}^{-3}$, the total number of droplets within the illuminated lidar volume is about 950k. Therefore, $p \sim 5\mathrm{k}/20\mathrm{k}/950\mathrm{k} \sim 10^{-7} \ll 1$. Theoretically, p can be larger if, for example, the lidar power is significantly increased. If so, the detector might be saturated, meaning that the received photon rate will be equal to the lidar repetition rate and the first-arriving photons within one time-gated window will all be from the first sublayer (i.e., $F(i)$ is a delta function), which is not the case based on our observations.

Because $A \equiv 1 - \delta < 1$ (Eq. (16)) and $p_i \ll 1$, if we keep terms on the order of $O(p_1)$ in the first bracket, Eq. (17) can be simplified to,

$$F(i) \approx \frac{\left(1-\sum_{s=1}^{i-1}A^{s-1}p_1\right)^n\left[1-(1-A^{i-1}p_1)^n\right]}{\sum_{j=1}^{m}\left(1-\sum_{s=1}^{j-1}A^{s-1}p_1\right)^n\left[1-(1-A^{j-1}p_1)^n\right]}. \tag{18}$$

Because $A = 1 - \delta$, and $\delta, p_1 \ll 1$, Eq. (18) can be further simplified to,

$$F(i) \approx \frac{\left[1-(i-1)np_1\right]\left[1-(i-1)\delta\right]np_1}{\sum_{j=1}^{m}\left[1-(j-1)np_1\right]\left[1-(j-1)\delta\right]np_1} \tag{19}$$

based on the Taylor expansion, $(1-x)^n \approx 1 - nx$ for $x \ll 1$. Because $np_1 \ll 1$ based on the T2 lidar observations (i.e., far from saturated), a first order approximation of the above equation (i.e., keep terms on the order of $O(np_1)$ results in,

$$F(i) \approx \frac{\left[1-(np_1+\delta)(i-1)\right]}{\sum_{j=1}^{m}\left[1-(np_1+\delta)(j-1)\right]}. \tag{20}$$

Finally, we can obtain Eq. (2),

$$F(i) \approx -\frac{2q}{2m - m^2q + mq}i + \frac{2+2q}{2m - m^2q + mq}, \tag{21}$$

where $q \equiv np_1 + \delta$ is the experimentally based parameter. Note that np_1 is analogous to the lidar backscattering coefficient[10], and the range-extinction parameter, $\delta \equiv 2(\sigma l + l/d)$, depends on the lidar extinction coefficient (σ, the product of particle concentration and single particle cross-section and extinction efficiency), thickness of the sublayer (l), and distance of the time-gated window from the lidar (d). Usually, $\sigma \gg 1/d$, and thus, $\delta = 2l(\sigma + 1/d) \approx 2\sigma l$ unless the clouds are so low that $\sigma \sim 1/d$.

Data availability

All data used in this study are archived in Digital Commons at Michigan Tech https://digitalcommons.mtu.edu/all-datasets/52/ (https://doi.org/10.37099/mtu.dc.all-datasets/52).

Code availability

The source codes for the analysis of this study are available from the corresponding author upon reasonable request.

Received: 1 December 2023; Accepted: 10 April 2024;
Published online: 20 April 2024

References

1. Lohmann, U. & Feichter, J. Global indirect aerosol effects: a review. *Atmos. Chem. Phys.* **5**, 715–737 (2005).
2. Bony, S. et al. Clouds, circulation and climate sensitivity. *Nat. Geosci.* **8**, 261–268 (2015).
3. Andreae, M. & Rosenfeld, D. Aerosol–cloud–precipitation interactions. Part 1. The nature and sources of cloud-active aerosols. *Earth Sci. Rev.* **89**, 13–41 (2008).
4. Baker, M. B. & Peter, T. Small-scale cloud processes and climate. *Nature* **451**, 299–300 (2008).
5. Rosenfeld, D., Sherwood, S., Wood, R. & Donner, L. Climate effects of aerosol-cloud interactions. *Science* **343**, 379–380 (2014).
6. Seinfeld, J. H. et al. Improving our fundamental understanding of the role of aerosol-cloud interactions in the climate system. *Proc. Natl Acad. Sci. USA* **113**, 5781–5790 (2016).
7. Glassmeier, F. et al. Aerosol-cloud-climate cooling overestimated by ship-track data. *Science* **371**, 485–489 (2021).
8. Ghan, S. J. et al. Droplet nucleation: physically-based parameterizations and comparative evaluation. *J. Adv. Model. Earth Syst.* **3**, M10001 (2011).
9. Twomey, S. Pollution and the planetary albedo. *Atmos. Environ.* **8**, 1251–1256 (1974).
10. Rap, A. et al. Natural aerosol direct and indirect radiative effects. *Geophys. Res. Lett.* **40**, 3297–3301 (2013).
11. Gunn, R. & Phillips, B. An experimental investigation of the effect of air pollution on the initiation of rain. *J. Atmos. Sci.* **14**, 272–280 (1957).
12. McFiggans, G. et al. The effect of physical and chemical aerosol properties on warm cloud droplet activation. *Atmos. Chem. Phys.* **6**, 2593–2649 (2006).
13. Ovadnevaite, J. et al. Surface tension prevails over solute effect in organic-influenced cloud droplet activation. *Nature* **546**, 637–641 (2017).
14. Topping, D. & McFiggans, G. Tight coupling of particle size, number and composition in atmospheric cloud droplet activation. *Atmos. Chem. Phys.* **12**, 3253–3260 (2012).
15. Reutter, P. et al. Aerosol-and updraft-limited regimes of cloud droplet formation: influence of particle number, size and hygroscopicity on the activation of cloud condensation nuclei (CCN). *Atmos. Chem. Phys.* **9**, 7067–7080 (2009).
16. Prabhakaran, P. et al. The role of turbulent fluctuations in aerosol activation and cloud formation. *Proc. Natl Acad. Sci. USA* **117**, 16831–16838 (2020).
17. Kreidenweis, S. M., Petters, M. & Lohmann, U. 100 years of progress in cloud physics, aerosols, and aerosol chemistry research. *Meteorol. Monogr.* **59**, 11–1 (2019).
18. Wang, Z. & Menenti, M. Challenges and opportunities in lidar remote sensing. *Front. Remote Sens.* **2**, 641723 (2021).
19. Yang, F. et al. A time-gated, time-correlated single-photon-counting lidar to observe atmospheric clouds at submeter resolution. *Remote Sens.* **15**, 1500 (2023).
20. Grosvenor, D. P. et al. Remote sensing of droplet number concentration in warm clouds: a review of the current state of knowledge and perspectives. *Rev. Geophys.* **56**, 409–453 (2018).
21. Zhao, C. et al. Toward understanding of differences in current cloud retrievals of ARM ground-based measurements. *J. Geophys. Res.* **117**, D10206 (2012).
22. Zhang, D. et al. Evaluation of four ground-based retrievals of cloud droplet number concentration in marine stratocumulus with aircraft in situ measurements. *Atmos. Meas. Tech.* **16**, 5827–5846 (2023).
23. Barton-Grimley, R. A., Stillwell, R. A. & Thayer, J. P. High resolution photon time-tagging lidar for atmospheric point cloud generation. *Opt. Express* **26**, 26030–26044 (2018).
24. Becker, W. *Advanced Time-correlated Single Photon Counting Applications*, vol. 111 (Springer, 2015).
25. Tosi, A. et al. Fast-gated single-photon counting technique widens dynamic range and speeds up acquisition time in time-resolved measurements. *Opt. Express* **19**, 10735–10746 (2011).
26. Buttafava, M., Zeman, J., Tosi, A., Eliceiri, K. & Velten, A. Non-line-of-sight imaging using a time-gated single photon avalanche diode. *Opt. Express* **23**, 20997–21011 (2015).
27. Kirmani, A. et al. First-photon imaging. *Science* **343**, 58–61 (2014).
28. Koren, I., Feingold, G., Jiang, H. & Altaratz, O. Aerosol effects on the inter-cloud region of a small cumulus cloud field. *Geophys. Res. Lett.* **36**, L14805 (2009).
29. Feingold, G. & Morley, B. Aerosol hygroscopic properties as measured by lidar and comparison with in situ measurements. *J.Geophys. Res.* **108**, 4327 (2003).
30. Korolev, A. V., Makarov, Y. E., Mazin, I. & V. S., N. On the droplet size distribution in layered stratiform clouds (in Russian). *Some Problems of Cloud Physics: Collected Papers* 143–159 (1986).
31. Kovalev, V. A. & Eichinger, W. E. *Elastic Lidar: Theory, Practice, and Analysis Methods* (John Wiley & Sons, 2004).
32. Ceolato, R. & Berg, M. J. Aerosol light extinction and backscattering: a review with a lidar perspective. *J. Quant. Spectrosc. Radiat. Transf.* **262**, 107492 (2021).
33. O'Connor, E. J., Illingworth, A. J. & Hogan, R. J. A technique for autocalibration of cloud lidar. *J. Atmos. Ocean. Technol.* **21**, 777–786 (2004).
34. Albrecht, B. A. et al. Surface-based remote sensing of the observed and the adiabatic liquid water content of stratocumulus clouds. *Geophys. Res. Lett.* **17**, 89–92 (1990).
35. Toledo, F., Haeffelin, M., Wærsted, E. & Dupont, J.-C. A new conceptual model for adiabatic fog. *Atmos. Chem. Phys.* **21**, 13099–13117 (2021).
36. E. Gerber, H., M. Frick, G., B. Jensen, J. & G. Hudson, J. Entrainment, mixing, and microphysics in trade-wind cumulus. *J. Meteorol. Soc. Jpn.* **86**, 87–106 (2008).
37. Davis, A. Multiple-scattering lidar from both sides of the clouds: addressing internal structure. *J. Geophys. Res.* **113**, D14S10 (2008).
38. Eloranta, E. W. *Calculation of Doubly Scattered Lidar Returns* (The University of Wisconsin-Madison, 1972).
39. Snider, J. R., Leon, D. & Wang, Z. Droplet concentration and spectral broadening in southeast pacific stratocumulus clouds. *J. Atmos. Sci.* **74**, 719–749 (2017).
40. Kostinski, A. Simple approximations for condensational growth. *Environ. Res. Lett.* **4**, 015005 (2009).
41. Korolev, A. V. & Mazin, I. P. Supersaturation of water vapor in clouds. *J. Atmos. Sci.* **60**, 2957–2974 (2003).
42. Pinsky, M., Mazin, I., Korolev, A. & Khain, A. Supersaturation and diffusional droplet growth in liquid clouds. *J. Atmos. Sci.* **70**, 2778–2793 (2013).
43. McComiskey, A. et al. An assessment of aerosol-cloud interactions in marine stratus clouds based on surface remote sensing. *J. Geophys. Res.* **114**, D09203 (2009).
44. Feingold, G., Walko, R., Stevens, B. & Cotton, W. Simulations of marine stratocumulus using a new microphysical parameterization scheme. *Atmos. Res.* **47**, 505–528 (1998).
45. Xue, H. & Feingold, G. A modeling study of the effect of nitric acid on cloud properties. *J. Geophys. Res.* **109**, D18204 (2004).
46. Yang, F., Shaw, R. & Xue, H. Conditions for super-adiabatic droplet growth after entrainment mixing. *Atmos. Chem. Phys.* **16**, 9421–9433 (2016).
47. Lu, C., Liu, Y., Xu, X., Gao, S. & Sun, C. Entrainment, mixing, and their microphysical influences. *Fast Processes in Large-Scale Atmospheric Models: Progress, Challenges, and Opportunities* 87–120 (2023).
48. Chin, H.-N. S. et al. A microphysical retrieval scheme for continental low-level stratiform clouds: Impacts of the subadiabatic character on

microphysical properties and radiation budgets. *Mon Weather Rev.* **128**, 2511–2527 (2000).
49. Braun, R. A. et al. Cloud adiabaticity and its relationship to marine stratocumulus characteristics over the northeast pacific ocean. *J. Geophys. Res.* **123**, 13–790 (2018).
50. Korolev, A. On the formation of non-adiabatic lwc profile in stratiform clouds. *Atmos. Res.* **29**, 129–134 (1993).
51. Schwartz, S. E., Huang, D. & Vladutescu, D. V. High-resolution photography of clouds from the surface: Retrieval of optical depth of thin clouds down to centimeter scales. *J. Geophys. Res.* **122**, 2898–2928 (2017).
52. Schröder, M. *Cloud Microphysics Investigations with the Cloudkite Laboratory*. Ph.D. thesis. (Georg-August-Universität Göttingen Göttingen, 2023).

Acknowledgements

We appreciate the three reviewers for their valuable comments. This project is funded by Brookhaven National Laboratory Program Development Award No. 20-012 and Laboratory Directed Research and Development Program award No. 21-039. An analytical model was developed by F.Y. and A.K. during their visit at KITP as part of the Multi-phase Flows in Geophysics and the Environment program. The cloud base n_d retrieval method was developed while R.A.S. was hosted as a sabbatical visitor at BNL. F.Y.'s KITP visit was supported in part by the National Science Foundation under grant No. NSF PHY-1748958. Z.Z. and A.M.V. were supported by the Biological and Environmental Research Program in the US Department of Energy, Office of Science, through contract No. DE-SC0012704 to Brookhaven National Laboratory. A.K. was supported in part by the NSF grant AGS-2217182, and R.A.S. was supported by NSF grant AGS-2133229.

Author contributions

F.Y. and A.B.K. conceived and designed the study. F.Y., P.H., Z.Z., E.L., and K.L. prepared the observations. F.Y., P.H., and Z.Z. conducted the observations. F.Y. and A.B.K. developed the theoretical models. F.Y. conducted numerical simulations. F.Y. and P.H. analyzed the data. F. Y., A.B.K., R.A.S., and A.M.V wrote the original paper. Z.Z., K.L., E.L., P.K., Y.M.S., and P.H. reviewed the paper.

Competing interests

The authors declare no competing interests.

Additional information

Supplementary information The online version contains supplementary material available at https://doi.org/10.1038/s41612-024-00644-y.

Correspondence and requests for materials should be addressed to Fan Yang.